Benchmark experiments for higher-order and full Stokes ice sheet models (ISMIP-HOM)

F. Pattyn, L. Perichon, A. Aschwanden, B. Breuer, B. de Smedt, O. Gagliardini, G. H. Gudmundsson, R. Hindmarsh, A. Hubbard, J. V. Johnson, et al.

The Cryosphere Discussions

Benchmark experiments for higher-order and full Stokes ice sheet models (ISMIP-HOM)[*]

F. Pattyn[1], L. Perichon[1], A. Aschwanden[2], B. Breuer[3], B. de Smedt[4], O. Gagliardini[5], G. H. Gudmundsson[6], R. Hindmarsh[6], A. Hubbard[7], J. V. Johnson[8], T. Kleiner[3], Y. Konovalov[9], C. Martin[6], A. J. Payne[10], D. Pollard[11], S. Price[10], M. Rückamp[3], F. Saito[12], O. Souček[13], S. Sugiyama[14], and T. Zwinger[15]

[1]Laboratoire de Glaciologie, Université Libre de Bruxelles, CP160/03, Av. F. Roosevelt 50, 1050 Brussels, Belgium
[2]Institute for Atmospheric and Climate Sciences, ETH Zurich, Universitaetstrasse 16, 8092 Zurich, Switzerland
[3]Institute for Geophysics, University of Muenster, Corrensstrasse 24, 48149 Muenster, Germany
[4]Vakgroep Geografie, Vrije Universiteit Brussel, Pleinlaan 2, 1050 Brussels, Belgium
[5]Laboratoire de Glaciologie et de Géophysique de l'Environnement (LGGE), CNRS, UJF-Grenoble I, BP 96, 38402 Saint Martin d'Hères Cedex, France

[*]Ice Sheet Model Intercomparison Project for Higher-Order Models; http://homepages.ulb.ac.be/~fpattyn/ismip

TCD

2, 111–151, 2008

Benchmarks for higher-order and full Stokes ice-sheet models

F. Pattyn et al.

Title Page

Abstract	Introduction
Conclusions	References
Tables	Figures

|◄ | ►|
◄ | ►
Back | Close

Full Screen / Esc

Printer-friendly Version

Interactive Discussion

[6]Physical Science Division, British Antarctic Survey, Natural Environment Research Council, High Cross, Madingley Road, Cambridge CB3 0ET, UK

[7]Centre for Glaciology, Institute of Geography and Earth Sciences, Aberystwyth University, Ceredigion, SY23 3DP, UK

[8]Department of Computer Science, Social Science Building Room 417, University of Montana, Missoula MT, 59812-5256, USA

[9]Moscow Engineering Physics Institute, Moscow, Russia

[10]Bristol Glaciology Centre, School of Geographical Sciences, University Road, University of Bristol, Bristol BS8 1SS, UK

[11]Earth and Environmental Systems Institute, College of Earth and Mineral Sciences, 2217 Earth-Engineering Sciences Bldg., Pennsylvania State University, University Park, PA 16802, USA

[12]Frontier Research Center for Global Change, 3173-25 Showamachi, Kanazawa-ku, Yokohama City, Kanagawa 236-0001, Japan

[13]Department of Geophysics, Charles University Prague, V. Holešovičkách 2, 18000 Praha 8, Czech Republic

[14]Institute of Low Temperature Science, Hokkaido University, Nishi-8, Kita-19, Sapporo 060-0819 Japan

[15]CSC-Scientific Computing Ltd., Keilaranta 14, P.O. Box 405, 02101 Espoo, Finland

Correspondence to: F. Pattyn (fpattyn@ulb.ac.be)

Title Page

Abstract | Introduction

Conclusions | References

Tables | Figures

◀ | ▶

◀ | ▶

Back | Close

Full Screen / Esc

Printer-friendly Version

Interactive Discussion

Benchmarks for higher-order and full Stokes ice-sheet models

F. Pattyn et al.

Full Screen / Esc

Abstract

We present the results of the first ice sheet model intercomparison project for higher-order and full Stokes ice sheet models. These models are validated in a series of six benchmark experiments of which one has an analytical solution under simplifying assumptions. Five of the tests are diagnostic and one experiment is prognostic or time dependent, for both 2-D and 3-D geometries. The results show a good convergence of the different models even for high aspect ratios. A clear distinction can be made between higher-order models and those that solve the full system of equations. The latter show a significantly better agreement with each other as well as with analytical solutions, which demonstrates that they are hardly influenced by the used numerics.

1 Introduction

According to the recent IPCC report (IPCC, 2007), dynamical processes related to ice flow not included in current models but suggested by recent observations could increase the vulnerability of the ice sheets to warming, increasing future sea level rise. Understanding of these processes is limited and there is no consensus on their magnitude. It was also stressed that a net ice mass loss could occur if dynamical ice discharge dominates the ice sheet mass balance (IPCC, 2007). Although the viscous flow of ice is rather well understood on a theoretical level, the reason for the lack of model confidence arises from the specification of stress boundary conditions and the lack of understanding of the processes at the base and the seaward margin. Here, several stress components come into play in regions of high variability in basal topography and/or basal slipperiness.

Despite the lack of comprehensive predictive ice-sheet modeling, the ice-sheet modeling community has evolved considerably over the last decade. Increasing computational power has led to the development of more complex ice sheet models, with varying degrees in approximations to the Stokes equations. There is a need for validating these

so-called higher-order models as analytical solutions are not always available. Similar benchmark exercises were done with large-scale ice sheet and ice shelf models in the 1990s (Huybrechts et al., 1996; MacAyeal et al., 1996; Payne et al., 2000), mostly based on zeroth-order approximations. Here, we present benchmark experiments that are validated by 28 ice-sheet models of varying degrees of complexity. Besides benchmarking, the experiments described in this paper also allowed for distinguishing under which conditions the approximations to the Stokes equations are viable and whether numerical issues play a role in the result.

During the first and second EISMINT[1] model intercomparison exercises, a number of benchmarks were proposed specifically for ice sheet models (Huybrechts et al., 1996, 1998; Payne et al., 2000) and ice shelf models (MacAyeal et al., 1996). These ice-sheet models were based on the zeroth-order "shallow-ice approximation" (SIA; Hutter, 1983), incorporating only vertical shear stresses in the force balance. The ISMIP–HOM exercise focuses on so-called higher-order models, i.e. models that incorporate further mechanical effects, principally longitudinal stress gradients, as well as those that solve the full system of equations of the linear Stokes problem.

The six experiments (A–F) presented in this benchmark are made accessible for many types of models, i.e. flowline models, vertically integrated planform models, as well as full three-dimensional models. They can be solved using a wide spread of numerical techniques, such as finite difference (FD), finite element (FE) or finite volume (FV). With exception of Exp. F, all experiments are diagnostic, i.e. time evolution is not considered. This means that for a given geometry of the ice mass, a Glen-type flow law and given appropriate boundary conditions, the stress and velocity field can be calculated. Exp. F considers time-dependent response (the experiment is run until the free surface and velocity field reach a steady state) for a constant viscosity (linear flow law). For this experiment analytical solutions exist (Gudmundsson, 2003). All thermomechanical effects are neglected and an isothermal ice mass is considered.

---

[1]EISMINT: European Ice Sheet Model INTercomparison; http://homepages.vub.ac.be/~phuybrec/eismint.html

Benchmarks for higher-order and full Stokes ice-sheet models

F. Pattyn et al.

2   General model setup

2.1   Model physics, parameters and constants

Higher-order models are any type of ice sheet or glacier model that incorporate further mechanical effects, principally longitudinal stress gradients apart from the two horizontal plane shear components (Hindmarsh, 2004). Such models are based on conservation laws of mass and momentum, i.e.

$$\nabla \cdot \mathbf{v} = 0 \, , \tag{1}$$

$$\rho \frac{d\mathbf{v}}{dt} = \nabla \cdot \mathbf{T} + \rho \mathbf{g} \, , \tag{2}$$

where ρ is the ice density, $\mathbf{g}$ gravitational acceleration, $\mathbf{v}$ the velocity vector, and $\mathbf{T}$ the stress tensor. Values for parameters and constants are given in Table 1. Generally, acceleration terms in Eq. (2) are neglected and ice incompressibility implies that the stress tensor is split into a deviatoric part and an isotropic pressure P,

$$\mathbf{T} = \mathbf{T}' - P\mathbf{I} \, . \tag{3}$$

The constitutive equation for ice then links deviatoric stresses to strain rates:

$$\mathbf{T}' = 2\eta \, \dot{\mathbf{e}} \, , \tag{4}$$

where $\mathbf{T}'$ and $\dot{\mathbf{e}}$ are the deviatoric stress and strain-rate tensor, respectively, and η is the effective viscosity. Both linear and nonlinear ice rheology is considered. In the latter case (Glen's flow law), η is strain-rate dependent and defined by

$$\eta = \frac{1}{2} A^{-1/n} \, \dot{\varepsilon}_e^{(1-n)/n} \, , \tag{5}$$

where $\dot{\varepsilon}_e$ is the second invariant of the strain rate tensor. For the linear rheology case, Eq. (5) reduces to $\eta = (2A)^{-1}$. The value for A is taken constant for the whole ice mass. Neglecting acceleration terms, the linear momentum balance is written as:

$$\text{div}\,\mathbf{T} + \rho_i \mathbf{g} = \text{div}\,\mathbf{T}' - \text{grad}\,P + \rho \mathbf{g} = 0 \, , \tag{6}$$

Title Page

Abstract | Introduction

Conclusions | References

Tables | Figures

◄◄ | ►►

◄ | ►

Back | Close

Full Screen / Esc

Since only acceleration due to gravity in the vertical is considered, this leads to

$$\frac{\partial \tau'_{xx}}{\partial x} - \frac{\partial P}{\partial x} + \frac{\partial \tau'_{xy}}{\partial y} + \frac{\partial \tau'_{xz}}{\partial z} = 0 \ , \tag{7}$$

$$\frac{\partial \tau'_{yx}}{\partial x} + \frac{\partial \tau'_{yy}}{\partial y} - \frac{\partial P}{\partial y} + \frac{\partial \tau'_{yz}}{\partial z} = 0 \ , \tag{8}$$

$$\frac{\partial \tau'_{zx}}{\partial x} + \frac{\partial \tau'_{zy}}{\partial y} + \frac{\partial \tau'_{zz}}{\partial z} - \frac{\partial P}{\partial z} = \rho g \ . \tag{9}$$

By definition the isotropic pressure is equal to $P = -\frac{1}{3} \sum_i \tau_{ii}$. Solving Eqs. (7–9) leads to the full Stokes solution. In higher-order models some simplifications are made to the above system of equations.

2.2 Boundary conditions

In Exps. A, B, E1 and F1 the ice is frozen to the bed ($\mathbf{v_b}$=0). For the other experiments, basal sliding is introduced through a friction law, characterized by a friction coefficient β^2. This friction law has the form of

$$\beta^2 \mathbf{t} \cdot \mathbf{v} = \mathbf{t} \cdot (\mathbf{Tn}_b) = \tau_b \ , \tag{10}$$

where $\mathbf{n}_b$ is the unit normal vector pointing into the bedrock, $\mathbf{t}$ the unit tangent vectors, and β^2 (Pa a m^{-1}) is a scalar quantity and always positive (MacAyeal, 1993). Basal shear stress τ_b is not equal to the driving stress, but part of the solution. At the surface of the ice mass (contact with air), a stress-free condition holds, which implies that $\mathbf{n}_s \cdot (\mathbf{Tn}_s) = P_{atm} \approx 0$.

Kinematic boundary conditions apply at the upper and lower surfaces of the ice mass, i.e.

$$\frac{\partial z_i}{\partial t} + v_x(z_i)\frac{\partial z_i}{\partial x} + v_y(z_i)\frac{\partial z_i}{\partial y} - v_z(z_i) = 0 \ , \tag{11}$$

for $i=(s, b)$. Since the vertical velocity field must obey the incompressibility condition (1), and the surface accumulation/ablation is zero ($M(s)=0$), the vertical velocity at the surface contains the local imbalance as well and becomes a model output.

2.3 Model domain

⁵ The model domain is square. The minimum number of grid points is not predefined and any type of discretization scheme can be used. Since this might be model dependent, the number of grid points in the horizontal as well as in the vertical direction can be chosen freely. The basic parameter for the experiments is the length scale of the domain L, that applies to both horizontal directions. Exps. A–D are carried out for
¹⁰ $L=160$, 80, 40, 20, 10 and 5 km, respectively, which results in aspect ratios $\epsilon=H/L$ varying between 0.006 up to 0.2. A scaled horizontal distance is introduced for output, varying between 0 and 1,

$$\hat{x} = \frac{x}{L} \qquad \hat{y} = \frac{y}{L} \ . \tag{12}$$

Periodic boundary conditions are applied to the horizontal boundaries, so that the sim-
¹⁵ ulation domain is surrounded with an infinite number of copies of itself in the horizontal.

3 Experiment description

3.1 Exp. A: ice flow over a bumpy bed

Exp. A considers a parallel-sided slab of ice with a mean ice thickness $H=1000$ m lying on a sloping bed with a mean slope $\alpha=0.5°$. This slope is maximum in x and zero
²⁰ in y. The basal topography is then defined as a series of sinusoidal bumps with an amplitude of 500 m (Fig. 1). The surface elevation is defined as

$$z_s(x, y) = -x \cdot \tan \alpha \ . \tag{13}$$

The basal topography is then given by

$$z_b(x, y) = z_s(x, y) - 1000 + 500 \sin(\omega x) \cdot \sin(\omega y) \ , \tag{14}$$

where $x \in [0, L]$ and L=160, 80, 40, 20, 10 and 5 km, respectively. The basal bumps have a frequency of $\omega = 2\pi/L$. The bed topography is shown in Fig. 2.

3.2 Exp. B: ice flow over a rippled bed

The only difference with Exp. A is that the basal topography does not vary with y, so that the experiment is suitable for 2-D flowline models as well. The basal topography is thus formed by a series of ripples with an amplitude of 500 m:

$$z_s(x, y) = -x \cdot \tan \alpha \tag{15}$$

$$z_b(x, y) = z_s(x, y) - 1000 + 500 \sin(\omega x) \ . \tag{16}$$

Width variations along the flow line are not considered.

3.3 Exp. C: ice stream flow I

The experiment setup is similar to Exp. A, albeit that the bedrock topography is flat, so that ice thickness remains constant for the whole domain (H=1000 m):

$$z_s(x, y) = -x \cdot \tan \alpha \tag{17}$$

$$z_b(x, y) = z_s(x, y) - 1000 \ , \tag{18}$$

where $x \in [0, L]$ and L=160, 80, 40, 20, 10 and 5 km, respectively, and where α=0.1°. The basal friction coefficient is prescribed as

$$\beta^2(x, y) = 1000 + 1000 \sin(\omega x) \cdot \sin(\omega y) \ . \tag{19}$$

The β^2-field is shown in Fig. 3. The basal friction bumps have a frequency of $\omega = 2\pi/L$.

Title Page

Abstract | Introduction

Conclusions | References

Tables | Figures

◄◄ | ►►

◄ | ►

Back | Close

Full Screen / Esc

Printer-friendly Version

Interactive Discussion

Benchmarks for higher-order and full Stokes ice-sheet models

F. Pattyn et al.

3.4 Exp. D: ice stream flow II

The only difference with Exp. C is that the basal friction coefficient does not vary with y, so that the experiment is suited for 2-D flowline models as well. The basal friction field is thus formed by a series of ripples defined as

$$\beta^2(x, y) = 1000 + 1000 \sin(\omega x) \ . \tag{20}$$

3.5 Exp. E: Haut Glacier d'Arolla

Exp. E is a diagnostic experiment along the central flowline of a temperate glacier in the European Alps (Haut Glacier d'Arolla), based on earlier experiments by Blatter et al. (1998) and Pattyn (2002). Input for the model is formed by the longitudinal surface and bedrock profiles of Haut Glacier d'Arolla, Switzerland, according to the Little Ice Age geometry (Fig. 4). The longitudinal profile of this glacier has a very simple geometry, hence the resulting stress field is not influenced by geometrical perturbations such as the presence of a steep ice fall. In a first experiment (E1), a zero basal velocity is considered ($\beta^2=\infty$), and the width of the drainage basin, is kept equal to 1 along the whole flowline domain. The flow-law rate factor A is taken constant over the whole model domain, and equals $A=10^{-16}\,\mathrm{Pa}^{-n}\,\mathrm{a}^{-1}$. Upstream and downstream boundary conditions imply a zero ice thickness and zero ice velocity. The input file has a resolution of $\Delta x=100\,\mathrm{m}$, but the authors were free to choose any grid/mesh resolution.

A second experiment (E2) considers a narrow zone of zero traction, similar to the experiment described in Blatter et al. (1998):

$$\beta^2 = 0 \qquad \text{for} \quad 2200 \le x \le 2500\,\mathrm{m}$$
$$\mathbf{v_b} = 0 \qquad \text{otherwise}$$

3.6 Exp. F: prognostic experiment

Exp. F is a prognostic experiment for which the free surface is allowed to relax until a steady state is reached for a zero surface mass balance:

$$\lim_{t\to\infty}\frac{\partial H}{\partial t} = \lim_{t\to\infty}\left[-\nabla_h\int_{z_b}^{z_s}\mathbf{v}_h dz\right] = 0 \, , \tag{21}$$

5 where $\mathbf{v}_h$ is the horizontal velocity vector (m a^{-1}). Basic model setup differs from the setup in Exps. A and C. For instance, a slab of ice with mean ice thickness $H^{(0)}$=1000 m is considered, resting on a sloping bed with a mean slope of α=3.0° (Fig. 5). This slope is maximum in x and zero in y. The bedrock plane is parallel to the surface plane and perturbed by a Gaussian bump. Initial bedrock $B^{(0)}$ and unperturbed surface $S^{(0)}$
10 elevation are thus governed by

$$S^{(0)}(x, y) = 0 \tag{22}$$

$$B^{(0)}(x, y) = -H^{(0)} + a_0\left(\exp\left[\frac{-(x^2 + y^2)}{\sigma^2}\right]\right) \, , \tag{23}$$

where σ=10 000=10$H^{(0)}$ and where x, y (m) are the horizontal coordinates with respect to the center of the Gaussian bump. The basal perturbation has a maximum height of
15 one tenth of the mean ice thickness, i.e. a_0=100=0.1$H^{(0)}$ (Fig. 5). The domain size L is taken 100 $H^{(0)}$ in x and y. The horizontal coordinates for output are scaled against σ by

$$\hat{x} = \frac{x}{H^{(0)}} \qquad \hat{y} = \frac{y}{H^{(0)}} \, . \tag{24}$$

Periodic boundary conditions are applied as well. The major difference with the previ-
20 ous experiments is that n=1 in Eq. (5), so that the effective viscosity is constant and

becomes $\eta = (2A)^{-1}$. Therefore, the unperturbed velocity field at the surface is defined by

$$U^{(0)} = AH^{(0)}\tau_b^{(0)} = \rho g A \left[H^{(0)}\right]^2 \sin \alpha \, , \qquad (25)$$

where $\tau_b^{(0)} = \rho g H^{(0)} \sin \alpha$ is the unperturbed basal shear stress, and $A = 2.140373 \times 10^{-7}\,\mathrm{Pa}^{-1}\,\mathrm{a}^{-1}$, so that $U^{(0)} = 100\,\mathrm{m\,a}^{-1}$.

Experiments are carried out for different values for slip ratios c, that determine the relation between the basal velocity and basal drag. The basal velocity is written in terms of a basal friction coefficient β^2, or

$$U_b = \frac{\tau_b}{\beta^2} \, . \qquad (26)$$

Following the scalings given by Gudmundsson (2003), the basal friction coefficient is related to the slip ratio c by

$$\beta^2 = \left(cAH^{(0)}\right)^{-1} \, . \qquad (27)$$

Experiments are run for slip ratios $c=0$ and 1 (F1 and F2, respectively). It is easily demonstrated that $U_b^{(0)} = cU^{(0)}$. Table 2 lists the main constants used for Exp. F. Using these settings, the model should run until a steady state of the free surface is reached.

4 Model classification

In total 27 numerical and 1 analytical model from 20 contributors participated in the intercomparison exercise. A list of model characteristics and contributions is summarized in Table 3. The different Stokes approximants all in some way start from the shallow ice approximation (SIA; Hutter, 1983; Hindmarsh, 2004). We will follow here the classification scheme for higher-order models by Hindmarsh (2004), who gives a

Title Page

Abstract | Introduction

Conclusions | References

Tables | Figures

◄ | ►

◄ | ►

Back | Close

Full Screen / Esc

Printer-friendly Version

Interactive Discussion

detailed description of the different "longitudinal stress schemes" widely used in ice sheet modeling. The most common longitudinal stress approximations introduce the two horizontal velocity components as field variables. This leads to an elliptic system with two rather than four variables of the full system at points in three-dimensional space (Pattyn, 2003; Hindmarsh, 2004), and the resultant linear systems are generally better conditioned than those resulting from the numerical analysis of the full system. These models are termed "multilayer models". A number of these models solve an elliptic system at one elevation only (generally the upper surface), and the resulting problem is therefore computationally two-dimensional. Besides the full Stokes system, approximations are labeled L1L1, L1L2, LMLa and LTSML (Hindmarsh, 2004).

The L1L1 approximation is a one-layer longitudinal stress scheme using τ'_{xx} at the surface computed by solving elliptic equations and identical to the approximation used by MacAyeal (1989). An alternative approximation is the L1L2 approach or one-layer longitudinal stress scheme using $\dot{\varepsilon}_{xx}$ at the surface computed by solving elliptical equations with a vertical correction of τ'_{xx}. Here, the surface velocities used in computing the non-horizontal plane stresses are computed using the shear stresses in the shear strain relationship and in the sliding relationship.

The most common approximation is the LMLa or multilayer longitudinal stress scheme. This is the classic longitudinal stress scheme as used by Blatter (1995) and Pattyn (2003). Compared with L1L2, the longitudinal stresses use the velocity at the corresponding elevations rather than at the surface, and the stress-invariant calculations are self-consistent rather than using the SIA stress (Hindmarsh, 2004). Finally, there is the LTSML or multilayer longitudinal stresses scheme with horizontal shear stress gradients approximated by SIA. Here, horizontal gradients of the vertical velocity are neglected. Horizontal plane shear stresses, when needed to calculate the horizontal gradient of such shear stresses, are approximated by SIA values. This approach is similar to an LMLa, but with inclusion of the vertical resistive stress R_{zz}, as used by Van der Veen and Whillans (1989).

5 Results

A graphical representation of all the results for each of the contributing authors as well as the submitted data files are found in the supplemental files (http://www.the-cryosphere-discuss.net/2/111/2008/tcd-2-111-2008-supplement.zip). An analysis of the CPU performance of each of the experiments is presented in an accompagning paper by Gagliardini and Zwinger.

5.1 Experiments A and B

The results for Exps. A and B are shown in Figs. 6 and 7, respectively. Each graph displays the surface velocity across the bumps at $y=L/4$ for Exp. A and along the central flowline for Exp. B, according to the different length scales and for the different participating models. The experiments were set up in such a way that for this longitudinal profile the SIA gives a solution that is completely independent of L, which is not the case for higher-order models. The surface velocity according to the SIA is given by

$$v_x(z_s) = v_x(z_b) + \frac{2A}{n+1} (\rho g \tan \alpha)^n H^{n+1} , \qquad (28)$$

where $v_x(z_b)=0$ is the basal velocity (Fig. 8). The maximum surface velocity according to the SIA remains constant for all length scales ($119.69\,\mathrm{m\,a^{-1}}$). However, whenever topographic differences occur, longitudinal stress gradients must develop which tend to smooth out the velocity field. For high aspect ratios $\epsilon=H/L$ (hence low values of L) this leads to a more or less constant surface velocity field as the ice sheet does not "feel" the individual bedrock undulations anymore. Rather, it feels the fast sequence of large bed undulations as a viscous drag. The aspect ratio ϵ determines the amplitude of the horizontal surface velocity field, and the surface velocity decreases from around 100 down to $10\,\mathrm{m\,a^{-1}}$ (Fig. 9).

Full Stokes models closely agree with each other when calculating the velocity field for different length scales, compared to the larger spread of solutions for the higher-order approximations. L1L1 and L1L2 models display by far the lowest accuracy. The

Title Page

Abstract | Introduction

Conclusions | References

Tables | Figures

◄ | ►

◄ | ►

Back | Close

Full Screen / Esc

Printer-friendly Version

Interactive Discussion

larger spread for LMLa, LTSML, L1L1 and L1L2 models is due to the fact that (i) more models are participating and that (ii) at the highest aspect ratios the different approximations are not valid anymore, so that the full stress field needs to be solved. For the smallest length scales the full Stokes models standard deviation reduces to <1% (Table 4).

The flowline experiments (Exp. B) show similar results as the 3-D experiments (Exp. A). Differences are related to the lack of developing transverse stress gradients and ice flow speeds are generally higher for the flowline case. A particularity is observed in the surface horizontal velocity for the smallest length scale L =5. The surface velocity according to all full Stokes models is larger over the bump than over the trough, hence anti-correlated with ice thickness (Fig. 7). All the other approximations (LMLa, LTSML, L1L2 and L1L1) predict a velocity to ice thickness correlation for all length scales. The marked difference can be attributed to mass conservation, as at such high aspect ratios the horizontal ice flux cannot be balanced anymore by the vertical flux at the free surface since the vertical velocity would be too large for the given depth. The horizontal ice flux is therefore more or less constant inducing larger velocities for smaller depth and vice versa. The feature is only noticeable for the flowline experiments as in 3-D the ice flow is allowed to flow around the bumps. The flow inversion is considered as an artifact stemming from the diagnostic nature of the experiments and would disappear if the free surface was allowed to respond to the applied stress field. Higher-order models fail to produce the velocity inversion, since the stress field is solely determined from horizontal strain rate components and vertical velocities are an a posteriori model result (e.g. Pattyn, 2003).

5.2 Experiments C and D

In this series of experiments, variations in basal conditions (slipperiness) determine when longitudinal stress gradients must develop. Due to the importance of basal sliding, the ice behaves as in an ice stream, in which vertical shearing is present, though minimal. Ice flow in this experiment can be considered as ice shelf flow with minimal

basal traction. The invalidity of the SIA solution is shown in Fig. 8, where the analytical SIA solution is plotted for a simplified basal sliding relationship in which the basal shear stress is supposed to balance the driving stress, hence without longitudinal stress gradients, so that

$$v_x(z_b) = (\rho g H \tan \alpha) \beta^{-2} , \tag{29}$$

in Eq. (28). However, a singularity occurs in Eq. (29) for $\beta^2=0$ (not all velocities are therefore plotted in Fig. 8). As for Exps. A and B, the SIA solution is independent of L. Again, full Stokes models are definitely more accurate than the higher-order approximations (Figs. 10–11 and Table 4). The SIA solution is definitely not suited for simulating this type of ice flow where longitudinal controls dominate over vertical shearing (compare with Fig. 8). Similar to the results of Exps. A–B, the amplitude of the surface velocity field decreases with increasing aspect ratio ϵ (Fig. 9). At the smallest length scales the surface velocity field is almost constant as the change between high and low friction areas is smoothed out due to longitudinal stress transmission. Similar to Exp. B, an inversion of the surface velocity field anti-correlated to basal friction is observed for full Stokes models and not for the other higher-order approximations (due to the larger disparity in solutions, this effect is unnoticeable in Fig. 11).

In general, the accuracy of the modeled velocity field is lower than for the experiments over the bumps. The highest accuracies are obtained with full Stokes models and the accuracy increases with increasing ϵ, contrary to the results from Exps. A–B. Accuracies for Exp. D are the lowest and the disparity of results is most pronounced for higher-order models. The results of L1L1 and L1L2 models lie the furthest away from the full Stokes solutions.

An apparent discontinuity in the model results and a difference between full Stokes and higher-order model solutions can be seen from the difference between the isotropic pressure at the base and the hydrostatic pressure P_H, i.e.

$$\Delta P(z_b) = P(z_b) - P_H(z_b) = -\frac{1}{3} \sum_i \tau_{ii}(z_b) - \rho g H \tag{30}$$

Benchmarks for higher-order and full Stokes ice-sheet models

F. Pattyn et al.

Title Page

Abstract	Introduction
Conclusions	References
Tables	Figures

|◀ | ▶|

◀ | ▶

Back | Close

Full Screen / Esc

Printer-friendly Version

Interactive Discussion

(Fig. 12). Contrary to the previous experiments, the discontinuity is not a function of aspect ratio, but most pronounced at a length scale $L=10$ km. It shows up at $x=3L/4$ and only for full Stokes models. However, the value of ΔP produced by the higher-order models is an a posteriori calculation, as by definition these models suppose hydrostatic approximation in the vertical, so that $\Delta P(z_b)=0$. Sudden changes in ΔP may occur when the ice flow changes from one regime to another, i.e. from no sliding to sliding and vice versa (see for instance Exp. E). However, in this series of experiments, changes in basal friction are smooth and even the high friction area is still dominated by basal sliding, as is the case for an ice stream. It is therefore not clear why the small bump in ΔP occurs in the full Stokes model solutions.

5.3 Experiment E: Haut Glacier d'Arolla

Although the input file lists the bedrock and surface data along the flowline of Haut Glacier d'Arolla with a fixed grid spacing of $\Delta x=100$ m, most participants interpolated this dataset at a higher resolution to obtain more accurate results (Fig. 13). The resolution dependence of the results is captured in Fig. 14, where the oscillations in the basal shear stress along the flowline are either jagged when undersampled or smoothed when a sufficiently small grid size is chosen. Most models simulate the surface velocity field along the flow line accurately, albeit that between higher-order model approximations the discrepancy is somewhat higher than for the full Stokes models.

Experiments with the sliding zone (area of zero basal friction) leads to much more discrepancy between the different participating models, and also the full Stokes models show a much larger range of solutions. Here, increasing resolution results in other caveats compared to the no-sliding case, such as the occurrence of oscillations in the basal shear stress. The slip/no slip boundaries are very sensitive to model resolution, as they can be regarded as singularities when the friction parameter β^2 suddenly jumps from zero to infinity and vice versa. Especially the linear interpolation that was applied leads to break points in basal and surface topography that influence the result. The results of the sliding experiment underline the difficulty to simulate end-member

behavior in basal sliding (no slip/slip).

5.4 Experiment F: prognostic run

Real benchmarking of numerical ice sheet models is only possible when analytical solutions for a particular problem exists. Furthermore, this experiment is the only time-dependent experiment and therefore very interesting to evaluate the transient behavior of the participating models. For this experiment, only few models participated, which underlines the present-day lack of time-dependent higher-order ice sheet models. The objective of the test was to run the models forward in time until a steady state was reached. The definition of steady state (precision at which no rate of change of variables in time is considered) was left to the interpretation of each participant. Results of the steady-state surface elevation and velocity are shown in Figs. 15–16.

The analytical solution is only available for a simple case, i.e. linear rheology and without basal sliding. The full Stokes numerical ice sheet models show a very good agreement with the analytical solution, although only two models are participating in the excercise. Higher-order model solutions fit also very well, but show a slightly larger variability, especially on behalf of velocities. This variability is emphasized when basal sliding is introduced. However, an analytical solution is lacking here. The fact that numerical solution of the full Stokes models lies closer to the analytical solution, compared to the higher-order solutions, is due the fact that both solve the same equations, which is not the case for the higher-order models.

6 Conclusions

In this paper we present the results of the first intercomparison exercise of higher-order and full Stokes ice sheet models. In total, 27 different numerical models participated in this benchmarking effort. A series of six experiments were designed to evaluate complex ice flow with high basal topographic variability and variations in slipperiness.

Title Page

Abstract | Introduction

Conclusions | References

Tables | Figures

|◄ | ►|

◄ | ►

Back | Close

Full Screen / Esc

Printer-friendly Version

Interactive Discussion

All experiments were designed in such a way that the Shallow-Ice Approximation (SIA) is not valid anymore, especially at high aspect ratios.

Compared to previous benchmark experiments (Huybrechts et al., 1996; MacAyeal et al., 1996; Payne et al., 2000), a significantly higher number of ice-sheet models participated in this benchmark, augmenting the representativity of the evaluation. Despite the higher complexity of the problem (compared to the SIA solution), all models produce results that converge even under extreme conditions of high aspect ratios. This shows that over the last decade numerical ice sheet models have improved considerably and are capable of simulating different types of ice flow, where longitudinal stress gradients are important.

As compared to full Stokes models, higher-order model approximations show a stronger deviation from the exact solution and a larger disparity. At least two reasons can be put forward. First, at high aspect ratios all stress components become important and the approximations offered by higher-order solutions are not sufficient. Second, most of the full Stokes models are NOT completely coded by the authors but rely for large parts on commercially available or open source software. Most of them are solved using finite elements. The results are therefore numerically more stable and accurate. The higher-order models on the other hand, are mostly solved using home-made code and are based on a wider variety of numerical methods. None of the participating models show real coding errors.

Although a limited number of L1L1 and L1L2 models participated, they perform generally better (larger spread in solutions) for basal topographic perturbations than for basal sliding perturbations, for which they were designed in the first place (i.e. simulating ice stream flow). LMLa models give valid results, but are significantly less accurate for very high aspect ratios or when basal sliding variability is important, compared to full Stokes models. All models (including full Stokes) poorly agree when sudden variations in basal friction are considered, such as the slip/no slip jumps in Exp. E.

Finally, the full Stokes models presented in this intercomparison give the most consistent results. They show a very low disparity of results and are well validated by the

analytical solution for linear rheology. For most experiments a clear distinction can be made between results from full Stokes and higher-order approximants, which gives us confidence that the solutions are less biased by numerical approaches than previous benchmarks experiments (Huybrechts et al., 1996).

References

Blatter, H.: Velocity and Stress Fields in Grounded Glaciers: a Simple Algorithm for Including Deviatoric Stress Gradients, J. Glaciol., 41, 333–344, 1995. 122, 134
15 Blatter, H., Clarke, G., and Colinge, J.: Stress and Velocity Fields in Glaciers: Part II. Sliding and Basal Stress Distribution, J. Glaciol., 44, 457–466, 1998. 119
Breuer, B., Lange, M., and Blindow, N.: Sensitivity Studies on Model Modifications to Assess the Dynamics of a Temperate Ice Cap, such as that on King George Island, Antarctica, J. Glaciol., 52, 235–247, 2006. 134
20 Colinge, J. and Rappaz, J.: A Strongly Nonlinear Problem Arising in Glaciology, Mathem. Modelling Numer. Analysis, 33, 395–406, 1999. 134
Gagliardini, O. and Zwinger, T.: The ISMIP–HOM Benchmark Experiments Performed Using the Finite-Element Code Elmer, The Cryosphere Discuss., 2, 75–109, 2008. 134
Gudmundsson, G.: Transmission of Basal Variability to a Glacier Surface, J. Geophys. Res.,
25 108(B5), 2253, doi:10.1029/2002JB002107, 2003. 114, 121, 134
Hindmarsh, R.: A Numerical Comparison of Approximations to the Stokes Equations used in Ice Sheet and Glacier Modeling, J. Geophys. Res., 109, F01012, doi:10.1029/2003JF000065, 2004. 115, 121, 122, 134
Hubbard, A., Blatter, H., Nienow, P., Mair, D., and Hubbard, B.: Comparison of a Three-

Dimensional Model for Glacier Flow with Field Data from Haut Glacier d'Arolla, Switzerland, J. Glaciol., 44, 368–378, 1998. 134

Hutter, K.: Theoretical Glaciology, Dordrecht, Kluwer Academic Publishers, 1983. 114, 121

Huybrechts, P., Payne, T., and The EISMINT Intercomparison Group: The EISMINT Benchmarks for Testing Ice-Sheet Models, Ann. Glaciol., 23, 1–12, 1996. 114, 128, 129

Huybrechts, P., Abe-Ouchi, A., Marsiat, I., Pattyn, F., Payne, T., Ritz, C., and Rommelaere, V.: Report of the Third EISMINT Workshop on Model Intercomparison, European Science Foundation (Strasbourg), 1998. 114

IPCC: Contribution of Working Group I to the Fourth Assessment Report of the Intergovernmental Panel on Climate Change, in: Climate Change 2007: The Physical Science Basis, edited by: Solomon, S., Qin, D., Manning, M., Chen, Z., Marquis, M., Averyt, K., Tignor, M., and Miller, H., p. 996, Cambridge University Press, Cambridge, United Kingdom and New York, NY, USA, 2007. 113

Johnson, J. and Staiger, J.: Modeling Long-Term Stability of the Ferrar Glacier, East Antarctica: Implications for Interpreting Cosmogenic Nuclide Inheritance, J. Geophys. Res., 112, F03S30, doi:10.1029/2006JF000599, 2007. 134

MacAyeal, D.: Large-scale Ice Flow over a Viscous Basal Sediment: Theory and Application to Ice Stream B, Antarctica, J. Geophys. Res., 94, 4071–4087, 1989. 122, 134

MacAyeal, D.: A Tutorial on the Use of Control Methods in Ice-Sheet Modeling, J. Glaciol., 39, 91–98, 1993. 116

MacAyeal, D., Rommelaere, V., Huybrechts, P., Hulbe, C., Determann, J., and Ritz, C.: An Ice-Shelf Model Test based on the Ross Ice Shelf, Ann. Glaciol., 23, 46–51, 1996. 114, 128

Martin, C., Navarro, F., Otero, J., Cuadrado, M., and Corcuera, M.: Three-dimensional Modelling of the Dynamics of Johnson Glacier (Livingstone Island, Antarctica), Ann. Glaciol., 39, 1–8, 2003. 134

Nienow, P., Hubbard, A., Hubbard, B., Chandler, D., Mair, D., Sharp, M., and Willis, I.: Hydrological Controls on Diurnal Ice Flow Variability in Valley Glaciers, J. Geophys. Res., 110, F04002, doi:10.1029/2003JF000112, 2005. 134

Pattyn, F.: Transient Glacier Response with a Higher-Order Numerical Ice-Flow Model, J. Glaciol., 48, 467–477, 2002. 119

Pattyn, F.: A New 3D Higher-Order Thermomechanical Ice-Sheet Model: Basic Sensitivity, Ice-Stream Development and Ice Flow across Subglacial Lakes, J. Geophys. Res., 108(B8), 2382, doi:10.1029/2002JB002329, 2003. 122, 124, 134

Benchmarks for higher-order and full Stokes ice-sheet models

F. Pattyn et al.

Pattyn, F.: Investigating the stability of subglacial lakes with a full Stokes ice sheet model, J. Glaciol., 54(185), in press, 2008. 134

Payne, A., Huybrechts, P., Abe-Ouchi, A., Calov, R., Fastook, J., Greve, R., Marshall, S., Marsiat, I., Ritz, C., Tarasov, L., and Thomassen, M.: Results from the EISMINT Model Intercomparsion: the Effects of Thermomechanical Coupling, J. Glaciol., 46, 227–238, 2000. 114, 128

Pollard, D. and DeConto, R.: A coupled ice-sheet/ice-shelf/sediment model applied to a marine-margin flowline: forced and unforced variations, in: Glacial Sedimentary Processes and Products, edited by: Hambrey, M., Christofferson, P., Glasser, N., and Hubbard, B., Blackwell Publishing, 2007. 134

Price, S., Waddington, E., and Conway, H.: A Full-Stress, Thermomechanical Flowband Model using the Finite Volume Method, J. Geophys. Res., 112(F03021), doi:10.1029/2006JF000725, 2007. 134

Sugiyama, S., Gudmundsson, G., and Ebling, J.: Numerical Investigation of the Effects of Temporal Variations in Basal Lubrications on Englacial Strain-Rate Distribution, Ann. Glaciol., 37, 49–54, 2003. 134

Van der Veen, C. and Whillans, I.: Force Budget: I. Theory and Numerical Methods, J. Glaciol., 35, 53–60, 1989. 122

Zwinger, T., Greve, R., Gagliardini, O., Shiraiwa, T., and Lyly, M.: A Full Stokes-flow Thermomechanical Model for Firn and Ice applied to the Gorshkov Crater Glacier, Kamchatka, Ann. Glaciol., 45, 29–37, 2007. 134

Title Page	
Abstract	Introduction
Conclusions	References
Tables	Figures

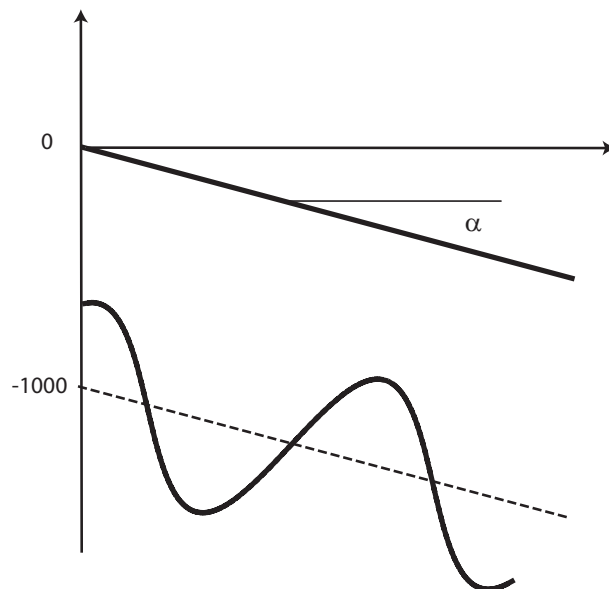| ◄◄	►►
◄	►
Back	Close

Full Screen / Esc

Printer-friendly Version

Interactive Discussion

Benchmarks for higher-order and full Stokes ice-sheet models

F. Pattyn et al.

Table 1. Constants for the numerical model.

	Constant	Value	Units
A	Ice-flow parameter	10^{-16}	$Pa^{-n}\,a^{-1}$
ρ	Ice density	910	$kg\,m^{-3}$
g	Gravitational constant	9.81	$m\,s^{-2}$
n	Exponent in Glen's flow law	3	
	Seconds per year	31 556 926	$s\,a^{-1}$

Benchmarks for higher-order and full Stokes ice-sheet models

F. Pattyn et al.

Table 2. Constants for the model setup according to Exp. F.

	Constant	Value
A	Ice-flow parameter	$2.140373 \times 10^{-7}\,\mathrm{Pa}^{-1}\,\mathrm{a}^{-1}$
n	Flow law exponent	1
α	Mean surface slope	3°
a_0	Amplitude Gaussian bump	$100\,\mathrm{m}$
σ	Width Gaussian bump	$10\,000\,\mathrm{m}$

TCD

2, 111–151, 2008

Benchmarks for higher-order and full Stokes ice-sheet models

F. Pattyn et al.

Title Page

Abstract	Introduction
Conclusions	References
Tables	Figures

◄◄ ►►

◄ ►

| Back | Close |

Full Screen / Esc

Printer-friendly Version

Interactive Discussion

Table 3. List with the 28 participating models. Model: model acronym based on the initials of each author; Type: the model type (see text for description); Dims: model dimensions; Method: numerical method (FE = finite elements, FD = finite differences, Sp = spectral method, FV = finite volume, An = analytical); A–F participation in the different experiments is marked with an ×.

Model	Type	Dims	Method	A	B	C	D	E	F	Reference
aas1	Full Stokes	2-D	FE		×		×	×		unpublished
aas2	Full Stokes	3-D	FE	×	×	×[a]	×			unpublished
ahu1	LMLa	3-D	FD	×[a]	×[a]	×[a]	×[a]	×		Hubbard et al. (1998); Nienow et al. (2005)
ahu2	LMLa	2-D	FD		×					Hubbard et al. (1998); Nienow et al. (2005)
bds1	LMLa	2-D	FE		×		×	×		unpublished
cma1	Full Stokes	3-D	FE	×	×	×	×	×	×	Martin et al. (2003)
cma2	LMLa	3-D	FE	×	×	×	×		×	unpublished
dpo1	L1L2	2-D	FD			×	×			Pollard and DeConto (2007)
fpa1	LMLa	3-D	FD	×	×	×	×	×	×	Pattyn (2003)
fpa2	Full Stokes	3-D	FD	×[c]		×[b]				Pattyn (2008)
fsa1	LMLa	3-D	FD	×	×	×			×	based on Pattyn (2003); Colinge and Rappaz (1999)
ghg1	Full Stokes	3-D	An					×[d]		Gudmundsson (2003)
jvj1	LMLa	3-D	FE	×[b]	×		×	×		Johnson and Staiger (2007)
lpe1	L1L1	2-D	FD			×				based on MacAyeal (1989); Pattyn (2003)
mbr1	LMLa	3-D	FD	×[b]	×[b]	×[c]	×[c]	×	×	Breuer et al. (2006)
mmr1	Full Stokes	3-D	FE		×	×	×	×		unpublished
mtk1	LTSML	3-D	FD	×	×				×	based on Blatter (1995); Hindmarsh (2004)
oga1	Full Stokes	3-D	FE	×	×	×	×	×	×	Zwinger et al. (2007); Gagliardini and Zwinger (2008)
oso1	SIA'	3-D		×[a]	×[a]					unpublished
rhi1	Full Stokes	3-D	Sp	×	×	×	×			Hindmarsh (2004)
rhi2	LMLa	3-D	Sp	×	×	×	×			Hindmarsh (2004)
rhi3	Full Stokes	3-D	Sp	×	×	×	×			Hindmarsh (2004)
rhi4	L1L2	3-D	Sp	×[a]	×[a]	×	×			Hindmarsh (2004)
rhi5	L1L1	2-D	Sp	×	×	×	×			Hindmarsh (2004)
spr1	Full Stokes	2-D	FV		×[a]			×[d]		Price et al. (2007)
ssu1	Full Stokes	2-D	FE		×		×	×		Sugiyama et al. (2003)
tpa1	LMLa	3-D	FD	×	×	×	×	×		based on Pattyn (2003); Hindmarsh (2004)
yko1	Full Stokes	3-D	FD	×				×[d]		unpublished

[a] not for $L = 5$ km
[b] not for $L = 5$ and 10 km
[c] not for $L = 5$, 10 and 20 km
[d] only no sliding case

TCD

2, 111–151, 2008

Benchmarks for higher-order and full Stokes ice-sheet models

F. Pattyn et al.

Title Page

Abstract | Introduction

Conclusions | References

Tables | Figures

|◄ | ►|

◄ | ►

Back | Close
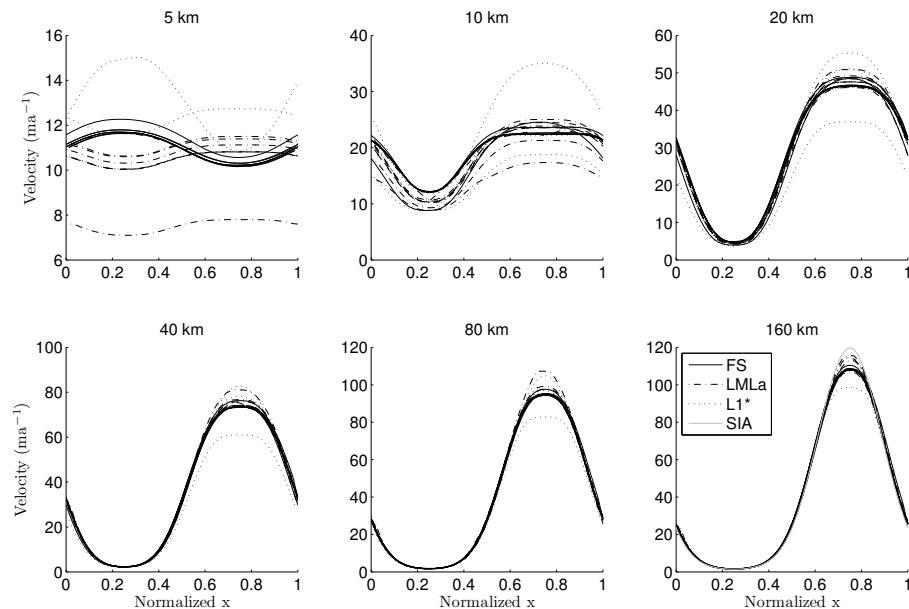
Full Screen / Esc

Printer-friendly Version

Interactive Discussion

Table 4. Mean values (μ), standard deviation (σ) and number of participating models (n) of the maximum horizontal ice velocity at the surface in the direction of the flow. Results are listed for Exp. A–D and for each length scale. Units are $m\,a^{-1}$.

L (km)	160 μ	(σ)	n	80 μ	(σ)	n	40 μ	(σ)	n	20 μ	(σ)	n	10 μ	(σ)	n	5 μ	(σ)	n
Exp. A																		
LM/L1	104.95	(5.11)	11	88.24	(2.21)	11	64.39	(4.79)	11	40.48	(3.67)	11	25.15	(3.36)	9	15.33	(1.76)	8
FS	105.45	(1.69)	7	88.99	(0.87)	7	65.06	(0.55)	7	40.46	(0.20)	6	24.56	(0.10)	6	14.71	(0.12)	6
Exp. B																		
LM/L1	109.30	(4.34)	14	96.34	(5.53)	14	74.90	(5.12)	14	47.77	(3.989)	14	23.46	(4.10)	13	11.40	(1.71)	11
FS	108.34	(0.84)	8	95.12	(1.01)	8	73.81	(0.99)	8	46.99	(1.01)	8	22.87	(0.80)	8	11.60	(0.52)	7
Exp. C																		
LM/L1	150.10	(19.45)	11	62.55	(3.51)	11	29.69	(3.51)	11	18.57	(0.59)	10	15.73	(1.02)	10	12.14	(5.22)	9
FS	145.82	(11.02)	7	60.37	(2.11)	7	29.09	(0.92)	7	19.10	(0.59)	7	16.52	(0.31)	6	15.99	(0.005)	5
Exp. D																		
LM/L1	229.79	(29.97)	12	92.72	(12.50)	12	40.49	(2.98)	12	20.60	(3.42)	11	16.01	(2.54)	11	13.26	(4.73)	10
FS	238.46	(1.30)	7	97.62	(1.61)	7	41.46	(1.00)	7	21.24	(0.55)	7	17.05	(0.27)	7	16.44	(0.14)	7

Fig. 1. Cartesian coordinate system used for Exp. A–D.
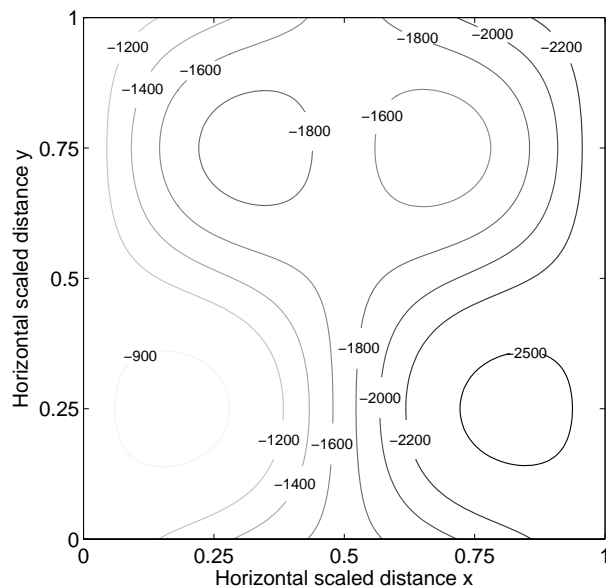
Fig. 2. Basal topography z_b (m) for Exp. A according to Eq. (14) for L=80 km. Ice flow is from left to right.
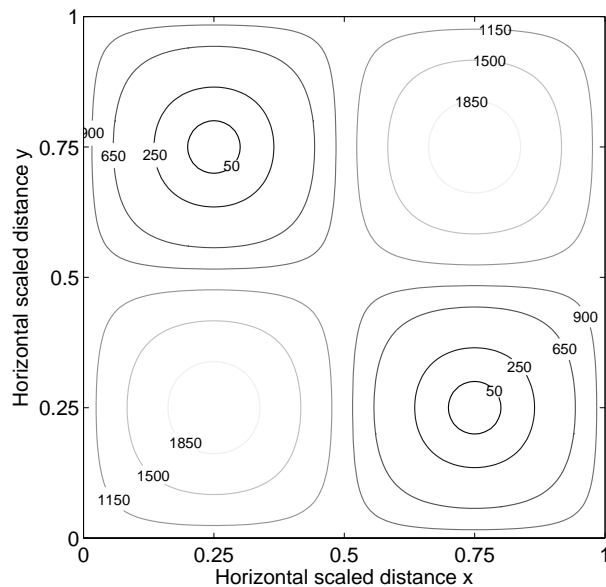
Fig. 3. Basal friction coefficient β^2 for Exp. C.

Fig. 4. Surface and bedrock profile of Haut Glacier d'Arolla.
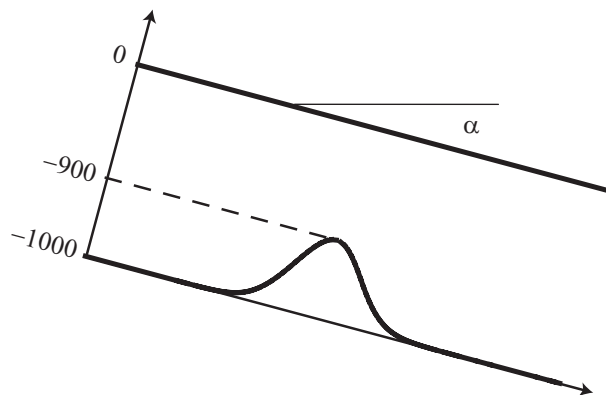
Full Screen / Esc

Fig. 5. Tilted coordinate system used for Exp. F.
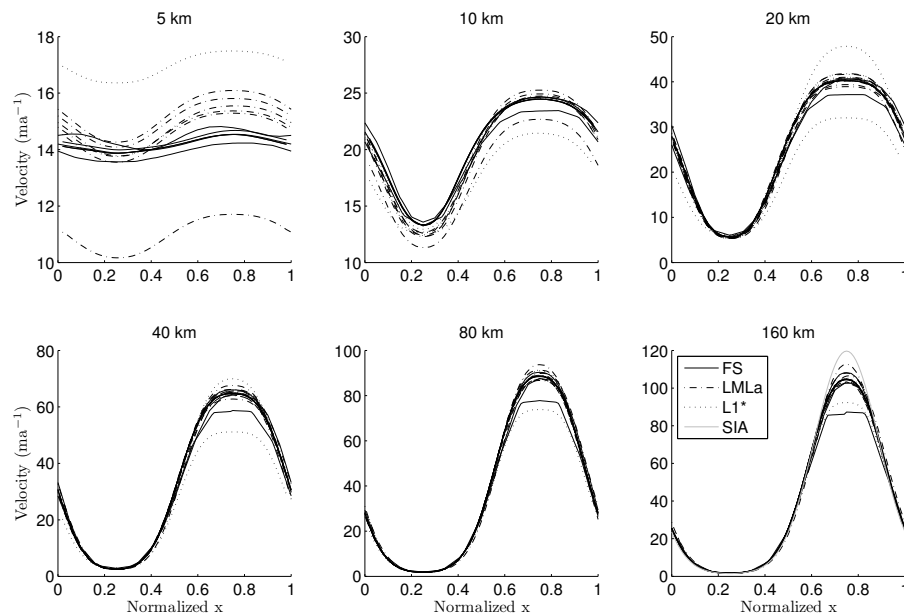
Fig. 6. Results for Exp. A. Surface velocity across the bump at $y = L/4$ for different length scales L.

Fig. 7. Results for Exp. B. Surface velocity for different length scales L.
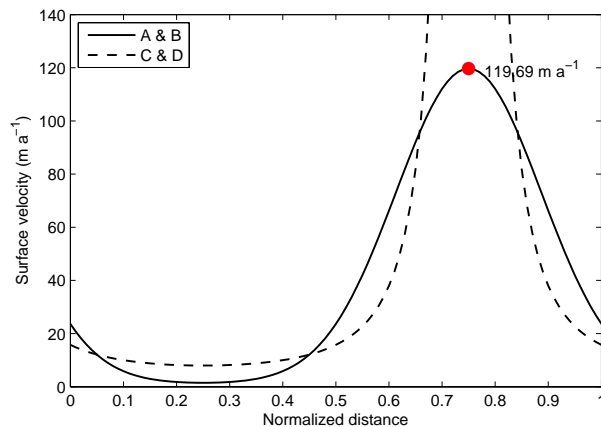
Fig. 8. Surface velocity profiles along $y=L/4$ according to the analytical SIA solution for Exps. A–D, based on Eqs. (28) and (29). Results are independent of L.
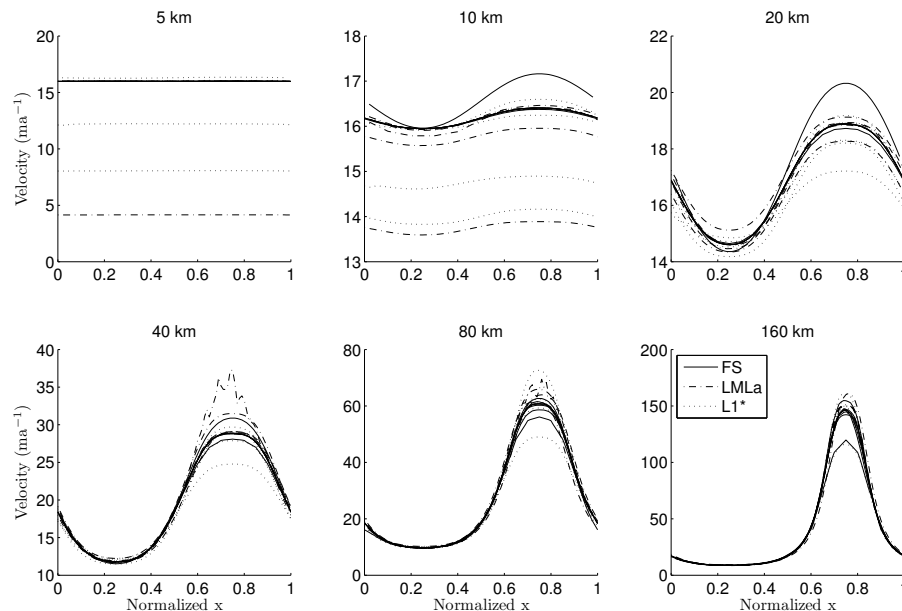
Fig. 9. Maximum surface velocity in the direction of the ice flow for Exp. A (top) and C (bottom) as a function of length scale L. Graphs for Exps. B and D are similar.
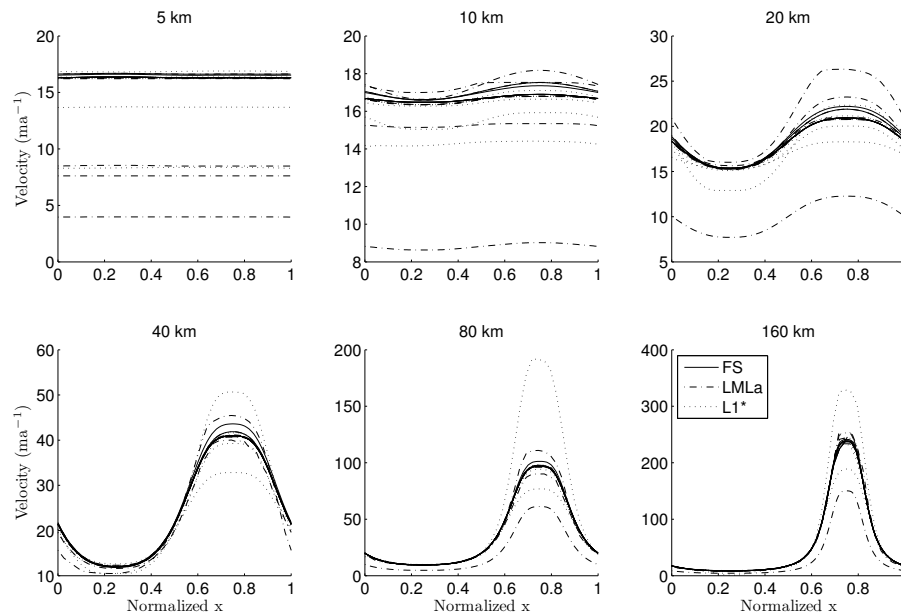
Fig. 10. Results for Exp. C. Surface velocity across the bump at $y=L/4$ for different length scales L.

Fig. 11. Results for Exp. D. Surface velocity for different length scales L.
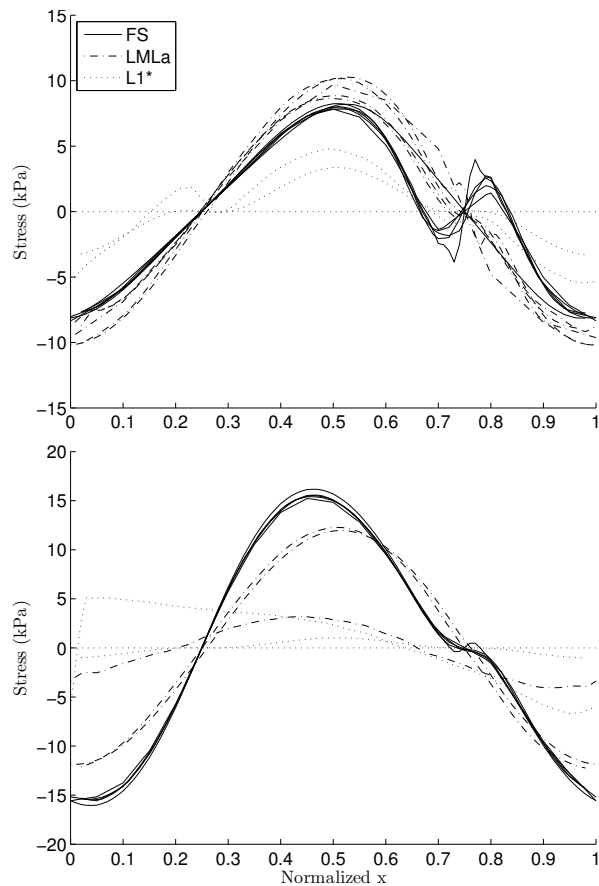
Fig. 12. Basal pressure difference according to Exp. C for $L = 10$ and 5 km, respectively.
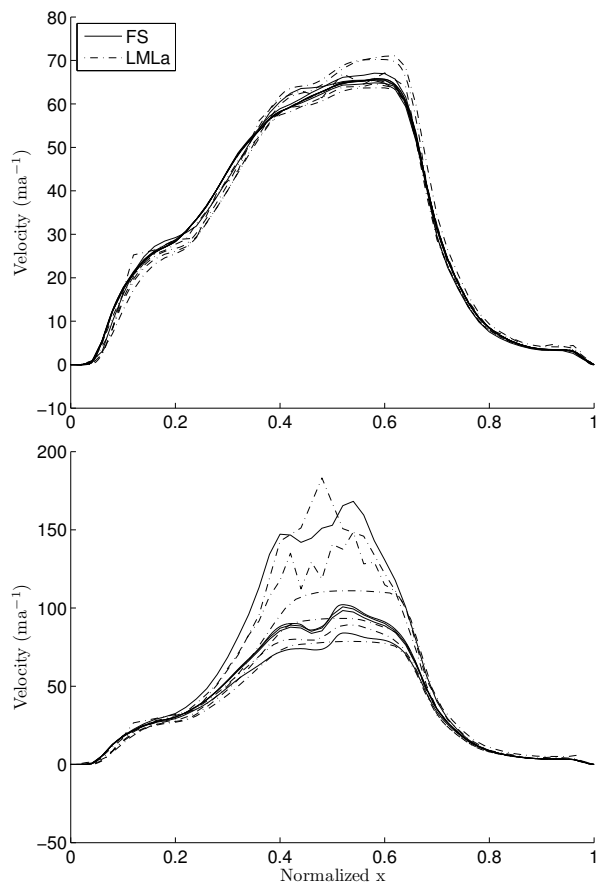
Fig. 13. Surface velocity in the direction of the ice flow for Exp. E for the no-sliding (top) and sliding (bottom) experiment.

Fig. 14. Basal shear stress in the direction of the ice flow for Exp. E for the no-sliding (top) and sliding (bottom) experiment.
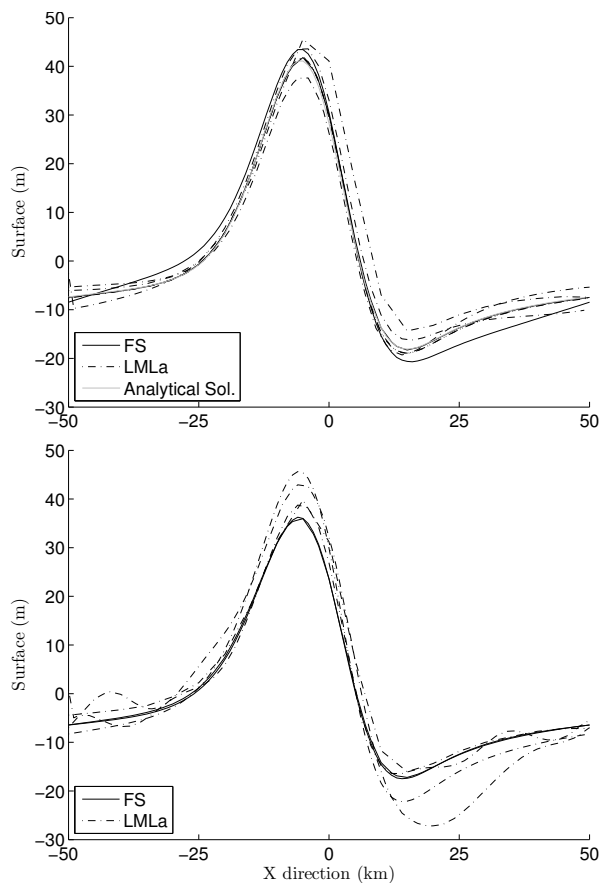
Fig. 15. Steady state surface elevation along the central flowline for Exp. F for the no sliding (top) and sliding (bottom) experiment.
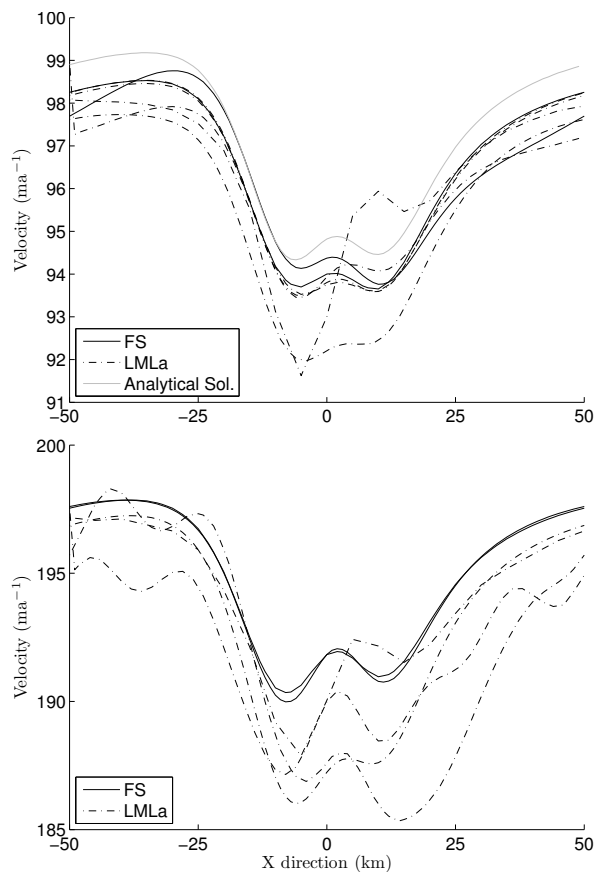
Fig. 16. Steady state surface velocity along the central flowline for Exp. F for the no sliding (top) and sliding (bottom) experiment.